arXiv:1512.05730v1 [astro-ph.GA] 17 Dec 2015

Accepted for publication in the Astrophysical Journal

Second Epoch Hubble Space Telescope Observations of Kepler's Supernova Remnant: The Proper Motions of Balmer Filaments[1]

Ravi Sankrit[2], John C. Raymond[3], William P. Blair[4], Knox S. Long[5], Brian J. Williams[6], Kazimierz J. Borkowski[7], Daniel J. Patnaude[3],

and

Stephen P. Reynolds[7]

ABSTRACT

We report on the proper motions of Balmer-dominated filaments in Kepler's supernova remnant using high resolution images obtained with the Hubble Space Telescope at two epochs separated by about 10 years. We use the improved proper motion measurements and revised values of shock velocities to derive a distance to Kepler of $5.1^{+0.8}_{-0.7}$ kpc. The main shock around the northern rim of the remnant has a typical speed of 1690 km s^{-1} and is encountering material with densities of about 8 cm^{-3}. We find evidence for the variation of shock properties over small spatial scales, including differences in the driving pressures as the shock wraps around a curved cloud surface. We find that the Balmer filaments ahead of the ejecta knot on the northwest boundary of the remnant are becoming fainter and more diffuse. We also find that the Balmer filaments associated with circumstellar material in the interior regions of the remnant are due to shocks with significantly lower velocities and that the brightness variations among these filaments trace the density distribution of the material, which may have a disk-like geometry.

---

[1]Based on observations made with the Hubble Space Telescope.

[2]SOFIA Science Center, NASA Ames Research Center, M/S N211-3, Moffett Field, CA 94035.

[3]Smithsonian Astrophysical Observatory

[4]Johns Hopkins University

[5]Space Telescope Science Institute

[6]CRESST/USRA and X-ray Astrophysics Laboratory, NASA GSFC

[7]North Carolina State University

Subject headings: ISM:individual objects(Kepler, SN1604, G4.5+6.8) – ISM:supernova remnants

1. Introduction

The historical supernova SN1604 was observed and documented by Johannes Kepler (Field et al. 1977). The supernova remnant (SNR) resulting from the explosion was discovered in a targeted search using the 100-inch reflector on Mt. Wilson "in the expectation that the ejected masses would still be visible" (Baade 1943).

Kepler's SNR (G4.5+6.8, hereafter Kepler) is located well away from the Galactic Plane, at a height of $590d_5$ pc, where d_5 is the distance to the remnant in units of 5 kpc. It shows up as a well-defined shell with a radius of about $2.6d_5$ pc in radio, X-ray (DeLaney et al. 2002) and infrared 24μm band (Blair et al. 2007) images. There is a pronounced asymmetry in the emission at these wavelengths, with the northern limb being much brighter than the southern limb. The contrast is more extreme in the optical, where filaments and knots extend across the northern and northwestern limb while the southern limb is not seen at all (Blair et al. 1991). The brightest optical emission is from a region in the northwest. Spectra of this bright emission show radiative shock emission arising from material with densities n_e of $\sim$1000 cm^{-3} (Dennefeld 1982; Leibowitz & Danziger 1983). These densities are much higher than expected for the interstellar medium at the location of Kepler, well off the plane of the galaxy, and therefore these measurements have been interpreted as evidence that the emitting gas is from the circumstellar medium (CSM) of the supernova progenitor system (Blair et al. 1991).

The supernova was classified as a Type I by Baade (1943) based on the reconstructed historical light curve, but that conclusion was called into question by Doggett & Branch (1985), who found that the light curve was equally consistent with a Type II-L supernova. The presence of nitrogen-rich circumstellar material (enhanced by $\sim$0.5 dex) appeared to favor a core-collapse origin (e.g. Bandiera 1987; Borkowski et al. 1992). However, Blair et al. (2007) pointed out that much of this nitrogen enhancement could arise simply from the galactic abundance gradient in the direction of Kepler, almost directly toward the galactic center. Its distance from the Galactic plane and X-ray spectral results (e.g. Kinugasa & Tsunemi 1999; Cassam-Chenaï et al. 2004) suggested that a Type Ia supernova was more likely. The debate over the supernova type was settled only with the analysis of a long (750 ksec) *Chandra* observation by Reynolds et al. (2007). Based primarily on the strong Fe emission and lack of O emission from the ejecta, they confirmed that Kepler was the result of a Type Ia supernova. More recently, Yamaguchi et al. (2014) reconfirmed the Type Ia

origin for Kepler based on the Fe K-shell emission observed with *Suzaku*.

In a few locations in Kepler, coincident with the bright radiative emission, Reynolds et al. (2007) detected oxygen emission and found solar O/Fe abundance ratios, which they associated with the shocked CSM. Burkey et al. (2013) carried out a detailed analysis of the *Chandra* data and found that the circumstellar material is primarily distributed around the bright north rim, but that substantial amounts of it are found projected near the center of the remnant. They follow Bandiera (1987) in explaining the bright northern rim as due to material piled up by the northward motion of the progenitor system, and they explain the centrally-projected CSM as a disk or torus of material seen edge-on.

The confirmation of its Type Ia origin, and the presence of the CSM imply that the progenitor system underwent significant mass loss prior to the explosion, and that the explosion most likely followed the single-degenerate scenario in which a white dwarf accretes matter from a non-degenerate companion, rather than the double-degenerate scenario in which two white dwarfs merge. Based on the structure and properties of the shocked CSM, several groups (Chiotellis et al. 2012; Burkey et al. 2013; Toledo-Roy et al. 2014) have modeled the progenitor system as a symbiotic binary, with the white dwarf accreting from an AGB star. In this scenario, the AGB wind shapes the CSM around the supernova. Strong silicate features detected in *Spitzer* IRS spectra of Kepler provide observational support for an AGB progenitor-companion as well (Williams et al. 2012). This companion, which should have survived the explosion, has so far not been discovered (Kerzendorf et al. 2014)

The distance to Kepler continues to be a matter of debate. Using a kinematic model of the galaxy, Reynoso & Goss (1999) placed a lower limit of 4.8 ± 1.4 kpc based on an H I absorption feature, and an independent upper limit of 6.4 kpc based on the lack of H I absorption from a known cloud. Our earlier work, described further below, used the proper motion of a Balmer filament and an estimated shock velocity to derive $d = 3.9^{+1.4}_{-0.9}$ kpc (Sankrit et al. 2005). In recent years, distances of either 4 or 5 kpc have been assumed in almost all the published literature on Kepler. However, simulations that combine the evolution of ejecta and the CSM seem to require that the distance be greater than 6 kpc if the explosion energy were 10^{51} ergs, the standard value for a Type Ia supernova (Chiotellis et al. 2012); a smaller distance to the remnant would require a sub-energetic Type Ia explosion. Patnaude et al. (2012) find that the amount of Fe in the X-ray spectrum indicates a larger than normal explosion energy for Kepler, which coupled with the CSM density profile in their model requires that the remnant be at a distance of at least 7 kpc.

Optical hydrogen Balmer filaments arise in regions just behind fast so-called non-radiative shock fronts where the pre-shock material is partly neutral. Charge exchange between neutral hydrogen atoms, which are unaffected by the shock, and shock-heated pro-

tons results in a population of fast neutrals. Some fraction of these atoms are excited and emit line photons before getting ionized (Chevalier & Raymond 1978). At this stage, the post-shock gas has not had sufficient time to recombine and cool via the emission of collisionally excited forbidden lines, and therefore, the strongest optical line by far is Balmer Hα. The Hα line thus has narrow and broad components arising from the neutrals at the pre-shock and post-shock gas temperatures, respectively. The width of the broad component is related to the shock velocity, albeit with various complications that have been examined recently (Morlino et al. 2013; Shimoda et al. 2015).

Spectra of Balmer filaments in Kepler were obtained by Fesen et al. (1989) and Blair et al. (1991), providing shock velocity estimates for a few positions. Proper motions of Balmer filaments have been measured by Sankrit et al. (2005), based on a comparison of a ground based image obtained in 1987 with one from the Hubble Space Telescope (HST) obtained in 2003. The low angular resolution of the ground based image and the crowded star field towards Kepler permitted us to measure the motion only at two locations near each other along a single filament in the northwest. In this paper, we present improved proper motion measurements of many Balmer filaments all around the SNR, using a second epoch of high angular resolution HST data with the first epoch HST data obtained nearly 10 years earlier. These measurements are used to improve the distance estimate to Kepler's SNR.

The second epoch observations and the procedure for aligning both epochs of images are described in §2. A brief overview of the optical emission from Kepler is given in §3, and the proper motion measurements of the Balmer filaments are presented in §4. The results and their implications for our understanding of Kepler's SNR are discussed in §5, and finally §6 contains a summary of the main results.

2. Observations, Data Processing and Image Alignment

Kepler was observed with the HST Wide Field Camera 3 (WFC3) between July 1 and 3, 2013, as part of a Cycle 20 Guest Observer Program (PID 12885). Observations were obtained in the UVIS channel through the narrow band filters F656N (9870 s) isolating Hα emission and F658N (3894 s) isolating [N II] λ6584 emission. Exposures through the largely line-free F547M filter were obtained and used for star alignment and astrometry. The images were centered on $\alpha_{J2000}, \delta_{J2000}$ = 17:30:40.8, −21:28:53.40. The WFC3/UVIS field of view, 162″ ×162″ is sufficient to include most of the optical emission from the remnant; only the eastern extremity of the northern limb, and the very faint filaments on the extreme western edge are outside the observed field of view. The observations were obtained using a standard dither and offset pattern in order to remove cosmic rays and hot pixels, fill in

the chip gaps, and to completely sample the PSFs. The Charge Transfer Efficiency (CTE) losses were minimized using an appropriate post-flash for each exposure to reach a pedestal of 12 electrons.

The data were processed using the DrizzlePac software suite (e.g., Fruchter et al. 2010; Gonzaga et al. 2012), as provided by STScI[1]. The exposures through each of the filters were corrected for CTE losses and then combined using the AstroDrizzle package. Alignment of the images was done using the TWEAKREG routine along with custom SExtractor star catalogs in each case. For images with a given filter, the RMS residuals are typically less than 0.05 pixels. In order to provide an absolute world coordinate system (WCS) frame, the WFC3 F547M was chosen as the reference filter and the drizzled image aligned to the 2MASS point source catalog [2]. The best fit gave RMS residuals of about 0.5 pixels (0.02″). The remaining WFC3 drizzled images were aligned with the F547M image, and the RMS residuals were about 0.05 pixels.

The first epoch HST observations were obtained with the Advanced Camera for Surveys (ACS) Wide Field Camera and have been described by Sankrit et al. (2008). Briefly, they consist of observations obtained through the following filters - F502N ([O III] λ5007), F658N (Hα+[N II] λ6584), F660N ([N II] λ6584) and F550M (line-free continuum). The ACS 202″ × 202″ field of view is larger than the WFC3 field, and was oriented differently. Also, the ACS/WFC pixels are 0.05″. The initial step to bring the images from both epochs to a common frame was to align the ACS F550M image with the WFC3 F547M reference image. Then, the remaining ACS images were aligned to the F550M image. Finally, the WCS solutions from the alignment procedures were propagated back using the TWEAKBACK routine and all images (epoch 1 and 2) were drizzled to a common 8500 × 8500 pix^2 grid with a WFC3/UVIS native pixel scale of 0.0396″, rectified to north up and east to the left. The images resulting from this final step are used in the figures, measurements and analyses presented in this paper.

3. Overview of the Optical Emission

The optical emission from Kepler is sparsely distributed. This is clearly seen by comparing X-ray and optical images of the remnant. Fig. 1a shows a *Chandra* image in the 4–6 keV band. The 270″ × 246″ field includes the entire remnant, and a near-complete shell is seen

[1]See http://drizzlepac.stsci.edu.

[2]available at http://www.ipac.caltech.edu/2mass/releases/allsky/

around its periphery. The emission in the band is predominantly non-thermal and arises from the shock interaction between the supernova blast wave and the interstellar medium (ISM). Fig. 1b is a *Spitzer* MIPS 24 μm image, deconvolved to an angular resolution $\approx 2''$ using ICORE (Masci 2013), and scaled to show the brightest emission. The larger box on the X-ray image outlines a trimmed $175'' \times 175''$ field for which the ACS F658N image is shown in Fig. 1c. In all three panels, the smaller boxes outline regions that will be discussed in the following sections.

The ACS image includes virtually all of the previously known optically emitting filaments and knots in Kepler (a few lie outside the field of view to the east-northeast and the west). The optical features consist of bright radiatively shocked knots that emit strongly in both Hα and [N II] and fainter non-radiative filaments that emit Hα only. The radiative emission is strongest in the region labeled "Box 1", where the blast wave is running into dense, clumpy circumstellar material. The fainter Balmer filaments produced by non-radiative shocks running into the ISM are seen along the northern rim. Spectra of the Balmer filaments (Fesen et al. 1989; Blair et al. 1991) show Hα line profiles consisting of narrow and broad components (FWHM ≈ 1750 km s^{-1}) confirming that the emission is due to shock excitation. Also along the rim is the shock created by an ejecta knot that has punched through the primary shock. The regions designated as "Wedge Filaments" and "Central Knots" contain emission from both radiative and non-radiative shocks. These regions appear to be part of a band running across the middle of the remnant, NW to SE. The band is clearly visible in the broad-band X-ray image presented by Burkey et al. (2013), who identified much of the emission with CSM material, and can be discerned in the *Chandra* image shown here in Fig. 1.

In the following sections we will focus on the evolution of the optically emitting material based on the two epochs of HST data. A thorough discussion of the optical emission from Kepler, including references to past work may be found in Sankrit et al. (2008).

4. Proper Motion Measurements

Figs. 2–8 show three-color images of the regions "Box 1", "Box 2", "Box 3", "Box 4", "Ejecta Knot", "Central Knots" and "Wedge Filaments". In each of these figures, the epoch 1 ACS F658N (Hα+[N II]) image is shown in red, the epoch 1 ACS F660N ([N II] only) image in blue and the epoch 2 WFC3 F656N (Hα only) in green. In the epoch 1 observations, the lack of emission in the [N II]–only image allows us to distinguish those filaments emitting only Hα. Any [N II] emission fainter than the F660N image background limit that may be included in the F658N data will have no effect on the measured displacements. In the figures,

the linear structures in red are the positions of the Balmer filaments in the epoch 1 images, and those in green are their positions in the epoch 2 data. Radiative shocks appear white or yellow, and stars appear white. Fig. 2 shows the region with the brightest radiative shocks. The edges to the knots and clumps appear red due to the much higher signal to noise of the ACS data compared with the WFC3 data, and due to the scaling which has been chosen to show the faint features.

The locations for measuring proper motions were chosen by eye, based on epoch 1, epoch 2 and combined 3-color images. The primary criterion for the selection was that linear features are identifiable at both epochs and are translated more or less in a perpendicular direction between epochs. For the final list of positions measured, we required a section of the filament at least 10 pixels wide free of contamination by stars or radiative knots in both epochs. The direction of the cross-cuts was also chosen by eye, but using an IDL routine where perpendicular lines were displayed and could be aligned with the filaments. The cross-cuts used are displayed in Figs. 2–8. For the primary shock front (Boxes 1, 2, 3, 4) these are labeled numerically starting with the westernmost position, and moving counter-clockwise around the remnant periphery.

The features corresponding to filaments are clearly identifiable in the cross-cuts. Two examples are shown in Fig. 9 - the top panel shows filament position 7 (Box 2), and the bottom panel shows the very faint filament 9 (Box 3). The alignment of the stars are also evident in these plots. The profiles from the two epochs were cross-correlated for a range of lags within some reasonable range. The cross-correlation vs. lag curve was fit by a quadratic, and the value of the lag corresponding to the cross-correlation minimum was taken to be the filament displacement. (The implementation was carried out using standard routines in IDL.) In order to check the error due to placement, we varied the angle of the cross-cuts by small amounts, and recalculated the lag minimizing the cross-correlation function and found that the measurements are accurate to about 0.5 pixels.

The proper motions in units of $''$/yr were determined from the measured displacement, using 0.0396 $''$/pixel and an elapsed time of 9.85 yr between the two epochs. The uncertainty in the proper motion for individual measurements is about 0.002 $''$/yr. The proper motions, along with other filament properties, are presented in Table 1. The first column is the filament label and the second gives the co-ordinates of the filament position in the epoch 1 ACS F658N image. The third column gives the box widths (in pixels) along the filaments used in generating the cross-cuts. The fourth column contains the measured proper motions in $''$/yr. The fifth and sixth columns contain the peak intensities and widths of the Hα filaments in the epoch 1 data. These values were obtained by fitting gaussians plus a linear background to the extracted profiles. The peak intensities in the table are in units of 10^{-16}

erg s^{-1} cm^{-2} arcsec^{-2}. The Data Numbers ($\bar{e}$/s/pixel) were converted to physical units by multiplying them by the inverse sensitivity, 1.96×10^{-18} erg/cm^2/Å/$\bar{e}$ and the filter width, 78.0Å (ACS Instrument Handbook, Table 5.1), and dividing by the area of a pixel, 1.57×10^{-3} arcsec^2. An important caveat is that the values for the peak intensities are only approximate since the conversion assumes a constant flux across the filter and does not account for the shapes and radial velocities of the Hα line. Most of the non-radiative shocks have widths (FWHM) of order 35Å, but a few are as wide as 80Å, and since about half the flux is in the broad component of the line, in these cases the filter profile may reduce the flux by up to 20%.

5. Discussion

5.1. Distance to Kepler's SNR

One of the goals of measuring Balmer filament proper motions is to combine them with independently determined shock velocities, for instance from Hα line widths (Chevalier & Raymond 1978; Ghavamian et al. 2007; van Adelsberg et al. 2008), and calculate the distance to Kepler. Under the assumption that we are viewing a shock edge-on, and that the observed filament traces the shock front at both epochs, the distance is given by

$$D(pc) = \frac{0.21\, v_{shock}(km\, s^{-1})}{\Delta\Theta('')/\Delta\, t(yr)} \tag{1}$$

and in the remainder of this paper, we will assume that this relationship is valid.

The Hα line widths of Balmer filaments have been measured in Kepler by Fesen et al. (1989) and Blair et al. (1991). Both studies targeted two positions, one in the NE, near filaments 12 and 13, and the other in the NW, near filaments 7 and 8. Fesen et al. (1989) obtained spectra with the slits running east to west, thereby cutting across the filaments. They reported FWHM values of 1750 ± 200 km s^{-1} for the broad Hα component at both locations. Blair et al. (1991) positioned the slits along the filaments, and estimated Hα broad component line widths of about 1620 km s^{-1} for the NE filament and 2330 km s^{-1} for the NW filament. The significantly larger line width measured for the NW position by Blair et al. (1991) may be due to contamination of the line profile by emission from other filaments in this complex region. Van Adelsberg et al. (2008) have used the Hα broad component width reported by Fesen et al. (1989) to infer a shock velocity of 1589^{+191}_{-182} km s^{-1} (see their Table 1). Morlino et al. (2013) give a different relation between shock speed and Hα width, but the difference is only significant for higher shock speeds.

For a given distance to the remnant, the shock velocity is proportional to the proper motion. The proper motions at positions 12 and 13 are the same – 0.06″, and those at positions 7 and 8 are about 10% and 25% larger (Table 1). Thus, the shock velocities among the positions will have a corresponding dispersion, which in turn should be reflected in the broad component widths of the Hα emission. Unfortunately, due to the relatively large error-bars in the spectra, the differences between the NE and NW filaments were not measurable, and in fact were reported to be the same value (Fesen et al. 1989). Therefore we are forced to make some assumption about which value of proper-motion corresponds best to the reported shock velocity. We assume that the shock velocity, 1589 km s^{-1} applies to the average proper motion measured at the four positions, 7, 8, 12 and 13, which equals 0.06575″/yr. Using these values we find D=$5.1^{+0.8}_{-0.7}$ kpc, where the error intervals are based on the uncertainties quoted above for the shock velocity and the error on a single measurement of the proper motion, which is 0.002″/yr (see §4).

Our newly derived distance to Kepler is significantly higher than our earlier estimate (Sankrit et al. 2005), which was based on the proper motion measurement of the NW filament (near positions 7 and 8 of this study). The difference is primarily due to the higher proper motion, $0.09 \pm 0.02''$/yr, used in the earlier study compared to the value used here. The current measurement of the NW filament proper motion is $\approx 0.07''$/yr, which is consistent (within the errors) with the earlier value. It is unlikely that the change in proper motion is due to deceleration of the filament. The decrease of the shock velocity by about 28% in 10 years would require an increase in the pre-shock density of about 65% in the same period. The gradient would have to be sufficiently smooth that the filament retains its linear morphology and does not show any significant changes in brightness. Typically, density contrasts are likely to be more clumpy - as evidenced by the example discussed in §5.2.1. The errors on the proper motion measurements reported in this paper are an order of magnitude lower than in the earlier study. Furthermore, the shock velocity adopted here, about 4% lower than used in our earlier study, benefits from the recent theoretical calculations of van Adelsberg et al. (2008). We conclude that our new value for the distance is more reliable than that obtained by Sankrit et al. (2005).

5.1.1. Caveat: Oblique Shocks

Recently, Shimoda et al. (2015) pointed out that shocks in a clumpy medium are rippled and mostly oblique, and that the obliquity can affect the relationship between the shock proper motion and the Hα line width. Their 3D hydrodynamic simulations indicated that the downstream temperatures as indicated by the Hα line widths are on average 24% below

those expected from the proper motions, which is to say that the Hα line width is 11% lower than would be expected from the proper motion. Hydrodynamic simulations of the effect of shock rippling on the Hα profiles could in principle be misleading in that shocks are typically spread over 3 to 5 cells, and the shock position must be chosen far enough back that the final temperature has been reached. However, Shimoda et al. (2015) have been careful to avoid such problems.

The prediction that the shock speeds corresponding to the proper motion exceed those derived from the Hα line width is somewhat counter-intuitive, because energy conservation implies that the shock energy is converted to the sum of thermal energy and turbulent kinetic energy, and if both thermal and turbulent velocities are isotropic the relation between line width and shock speed must be the same as in a planar shock. Shimoda et al. (2015) attribute the lower line widths to anisotropic turbulence. Another possibility is that the shock moves most rapidly through the low density regions and "heals" after it crosses a small high density region. In that case, the proper motion would correspond to the faster shock speed, while the Hα line width would be an average of high and low speeds.

It is somewhat surprising that the density contrast of a few percent expected in the ISM at the relevant scales could produce as large an effect as reported by Shimoda et al. (2015), but the irregularity of the shock surface and the presence of both radiative and non-radiative shocks indicate a very high level of density fluctuations in the CSM of Kepler. Thus the effects of shock rippling should be much stronger than in remnants such as Tycho or SN1006. One estimate of the level of irregularity of the shock surface is the ratio of the thickness of a filament to its length. As seen in Figure 2, the straight segments of the filaments are typically $5''$ long, while the thicknesses listed in Table 1 are about $0.2''$, for typical ratios of 25. By comparison, the Hα filaments in the NW section of SN1006 have lengths of arcminutes and thicknesses of about $0.3''$, for a ratio of over 200 (Raymond et al. 2007). Moreover, the filament thickness in SN1006 corresponds to the angular ionization length scale of H I (Heng et al. 2007), while the angular ionization length scale in Kepler is about 10 times smaller due to its higher densities, lower shock speeds and larger distance. Therefore, the thickness of the SN1006 filaments is only an upper limit to the amplitude of shock ripples, while in Kepler it may be due to either curvature on the scale of the filament length or to smaller scale rippling.

We conclude that because of the strong density fluctuations in thefuther pre-shock medium of Kepler's SNR, care will be needed in using the proper motions and shock speeds from Hα profiles to obtain the distance. Some handle on the effects of rippling can be obtained simply by looking at the scatter among distances derived from different filaments. We defer further analysis until we have a larger set of Hα line widths for the filaments whose

proper motion we have measured.

The distance of 5.1 kpc to Kepler will be a modest overestimate if the shock velocity from the Hα line width is lower than that from proper motion.

5.2. Shock Velocities and Intensities

For a distance of 5.1 kpc the proper motion shock velocity is given by: $v_s(km\,s^{-1}) \approx 24300 \times \Delta\Theta/\Delta\,t(''/\mathrm{yr})$. The error of 0.5 pix in the measured displacement of the filaments translates to an error in the shock velocity of about 50 km s^{-1}. Fig. 10 shows a plot of the Hα fluxes per arcsecond length along the filament versus shock speed. The fluxes are derived from the Gaussian fits (Table 1) as $I_{peak} \times FWHM \times 1.064$.

For a non-radiative shock with depth L along the line of sight, shock velocity v_s, pre-shock density n_0, and neutral fraction f_{neut}, the flux (uncorrected for interstellar extinction) is

$$F = \frac{N_{H\alpha}\, n_0\, f_{neut}\, v_s\, L\, h\nu}{4\pi}\ erg\ cm^{-1}\ s^{-1}\ sr^{-1} \tag{2}$$

where $N_{\mathrm{H}\alpha}$=0.25 is the number of Hα photons per neutral H atom (Laming et al. 1996) and $h\nu = 3.03 \times 10^{-12}$ erg is the photon energy. We use the reddening to Kepler, E(B-V)=0.9 (Blair et al. 1991) and R_V=3.1 to obtain an extinction $A_{\mathrm{H}\alpha} = 2.27$. Using appropriate values for the parameters and correcting for the interstellar extinction yields

$$F = 0.9 \times 10^{-16} n_0 f_{neut} v_{1000} L_{17.6}\ erg\ cm^{-2}\ s^{-1}\ arcsec^{-1} \tag{3}$$

where v_{1000} is the shock speed in units of 1000 km s^{-1}, and $L_{17.6}$ is the line of sight depth in units of 4×10^{17} cm, corresponding to the 5″ length typical of the filaments. The neutral fraction is not known, but has been estimated at 0.1 for non-radiative shocks in SN1006 (Ghavamian et al. 2002), 0.8 for Tycho (Ghavamian et al. 2001) and 0.06–0.2 for the Cygnus Loop (Raymond et al. 2013). In Kepler it is likely to be small in filaments close to radiative shocks, but may vary significantly from one location to another.

5.2.1. The Main Shock

The proper motion shock velocities for the main shock positions, shown as diamonds in Fig. 10, range from 1190 km s^{-1} (position 11) to 2280 km s^{-1} (position 9). The fluxes of all but two of the positions (2 and 5) lie between 0.44 and 3.24×10^{-16} erg s^{-1} cm^{-2} arcsec^{-1}.

Excluding these outliers, the median shock speed is 1690 km s^{-1} and the median flux is 1.21×10^{-16} erg s^{-1} cm^{-2} arcsec^{-1}, which imply that if $f_{neut} = 0.1$ and $L_{17.6} = 1$, then the shocks are encountering densities of about 8 cm^{-3}. This is consistent with the post-shock density of 42 cm^{-3} derived from IR spectroscopy by Williams et al. (2012) for a region in the northern part of the remnant (within Box 3 of this paper).

Positions 2 and 5 have shock velocities of 1340 and 1410 km s^{-1}, respectively, which are about 20% lower than the median value, but fluxes that are about 5.5 and 4.5 times the typical value. There is evidence for hotter dust in these regions from ISOCAM 14–16 μm data (Douvion et al. 2001) and *Spitzer* IRS spectra (Williams et al. 2012). The higher dust temperatures indicate higher densities. Since the shock velocities at positions 2 and 5 are typical, the brightness and higher densities suggest that the driving pressures are significantly higher than average at these locations. Position 2 is close to the apex of a curved structure (Fig. 2) where the blast wave seems to be wrapping around a cloud. In this case, significant pressure variations are expected (Borkowski et al. 1997). There is no similar morphological evidence at position 5, but significant pressure variations are expected even on small spatial scales. We may turn the argument around and argue that the shock velocity and brightness of the filament at position 5 implies a higher pressure at that location.

The variation in shock properties between positions 3 and 4 is noteworthy. They lie on the same filament and are separated by about 0.7″ (Fig. 2). The shock speed at position 3 is 1770 km s^{-1}, and at position 4 it is 1970 km s^{-1}. It is likely that the shock is slower at position 3 due to a higher density clump in the pre-shock gas. If the driving pressure, $n_0 v_s^2$ is the same at both locations, then the density contrast is about 25%. However, the flux at position 3 is almost 6 times higher than at position 4. A straightforward explanation is that the neutral fraction in the dense clump is higher by a factor of 5 compared with its surroundings.

An extreme variation in shock velocity over a small scale occurs between positions 10 and 11, which are separated by only 0.7″ (Fig. 4). The appearance of the region clearly shows complex changes between epoch 1 and 2. The shock velocities at the two positions are 2140 and 1190 km s^{-1}, respectively. Assuming $f_{neut} = 0.1$ and $L_{17.6}$=1 for both positions, equation 3 yields densities of 6.0 and 16.3 cm^{-3} for positions 10 and 11. These values are consistent with the driving pressure being the same (to within 15%) at the two positions.

5.2.2. The Ejecta Knot

The Ejecta Knot (Fig. 6) first appeared *ca.* 1970 (van den Bergh & Kamper 1977) and brightened rapidly until by 1985 its Hα+[N II] intensity was comparable to the brightest regions in the remnant (Dodorico et al. 1986). The detailed structure of the region was revealed by our first epoch HST images (Sankrit et al. 2008) as consisting of arc-shaped Balmer dominated filaments tracing a shock front and trailing radiative knots due to Rayleigh-Taylor like instabilities. The clear correlation between the emitting structures in the X-ray and in Hα may be seen in Fig. 11. The deep (750 ks exposure) *Chandra* data used for the image was analyzed by Reynolds et al. (2007) and Burkey et al. (2013) who showed that the emission was from a knot of ejecta rather than a dense clump in the CSM.

Between epoch 1 and 2, the sharply defined filaments have become more diffuse. This is most clearly seen for Ej4 (Fig. 6, where the filament position is poorly defined in the 2013 image, and consequently only an approximate value of the proper motion is reported (Table 1).

Positions on the shock front ahead of the Ejecta Knot are shown as thick crosses in Fig. 10. The fastest moving is position Ej3, where the shock velocity is 2960 km s^{-1}, significantly higher than any of the main shock positions. The shock velocities at the remaining three positions fall within the main shock range, and are biased towards higher values. The flux at Ej3 is 1.03×10^{-16} erg s^{-1} cm^{-2} arcsec^{-1}, and $L_{17.6} \approx 0.25$ (Fig. 6), which yield $n_0\, f_{neut} = 1.5\,\mathrm{cm}^{-3}$. The neutral fraction in the pre-shock gas ahead of the ejecta knot is unknown, but could plausibly be higher than the value of 0.1 assumed for the main shock. The extreme case of $f_{neut} = 1.0$ implies that $n_0 = 1.5\,\mathrm{cm}^{-3}$.

5.2.3. The Central Knots and Wedge Filaments

The central knots comprise Balmer dominated filaments due to non-radiative shocks and radiatively shocked knots interspersed among each other within a small area (Fig. 7). The optical emission is blue-shifted relative to the mean radial velocity of Kepler (Blair et al. 1991). The X-ray emission from the region correlates well with the Hα emission (Fig. 12). Burkey et al. (2013) have shown that the X-ray emission from the region is primarily from circumstellar material. This may be seen by comparing the X-ray image of the Central Knots region with that of the NE limb shown in Fig. 11. Both images have been scaled identically, and the redder appearance of the central knots is due primarily to oxygen lines, characteristic of the CSM.

The Hα emission morphology is complex, and although a number of changes between the

two epochs are evident (Fig. 7), unambiguously identifying filaments that trace the motion of shock fronts is difficult. We have isolated two positions, C1 and C2, that plausibly do represent real filament motion. We note that the filaments lying to the southwest of C1 that appear green in Fig. 7 are not newly emerged in epoch 2; they are clearly visible in the epoch 1 data, but due to the stretch used in the display are not seen in the image presented.

The wedge filaments (Fig. 8) are a pair of linear Balmer filaments that define a wedge-shaped structure, which is located well inside the projected boundary of the remnant (Fig. 1). The morphology suggests that the primary shock encountered an inward protrusion and wrapped around its sides, and the filaments are the tangencies of the shock front along the line of sight. Proper motions could be measured at three adjacent locations (WF1, WF2 and WF3) on the brighter southern filament, whereas a very wide box was necessary to get sufficient counts for the measurement on the fainter northern side.

In Fig. 10 thick 'X's show the positions in the central region, and filled circles those on the wedge filaments. The shock velocities at positions C1 and C2 are 580 and 730 km s^{-1}, respectively, and the fluxes are 4.79 and 2.73×10^{-16} erg s^{-1} cm^{-2} $arcsec^{-1}$. Assuming f_{neut}=0.1, and $L_{17.6} = 0.2$ based on the 0.8″ filament length (Fig. 7), we obtain pre-shock densities of about 460 and 220 cm^{-3} at the two locations.

The shock velocities for the wedge filament positions all lie in a narrow range 700–930 km s^{-1}. The fluxes along the southern side show a systematic decrease away from the thin edge of the wedge, falling from 3.70 to 1.28×10^{-16} erg s^{-1} cm^{-2} $arcsec^{-1}$ between WF1 and WF3. The northern side is fainter still with a flux 0.36×10^{-16} erg s^{-1} cm^{-2} $arcsec^{-1}$. The gradient along the southern side may be due to a density gradient. The difference between southern and northern sides is probably caused by the geometry of the wedge. One scenario that explains the contrast in brightness is that the northern shock front is inclined to the line of sight, and therefore the length through the emitting region is small. This would also imply that the proper motion shock speed is an underestimate of the true shock speed. The current data are not sufficient to distinguish between this and other possibilities.

Burkey et al. (2013) have shown that the regions around the central knots and wedge filaments are dominated by material from the progenitor CSM (see their Fig. 2). Their model of SN ejecta with an exponential profile expanding into an azimuthally varying stellar wind results in a torus of shocked CSM occupying the equatorial plane. In the context of this model, the Balmer filaments in the central knots region and the wedge filaments are shocks being driven into this torus. The shock velocity and Hα intensity measurements thus provide quantitative information that can constrain more detailed models of the shock-CSM interaction in Kepler's SNR.

6. Concluding Remarks

We have presented HST images of Kepler's SNR obtained approximately ten years apart and measured the proper motion of the Balmer filaments, which trace non-radiative shocks. This study represents a significant improvement over that of Sankrit et al. (2005) – in the current study 26 filament positions were accessible for measurement as compared with two in the earlier work, and the statistical errors on the measurements were reduced by an order of magnitude. We used the average proper motion for four filament positions and the shock velocity reported in the literature to obtain a distance of 5.1 kpc to Kepler, which is about 30% higher than the value obtained by Sankrit et al. (2005). The higher value reduces, but does not altogether eliminate, the tension between the distance obtained using Balmer filament proper motions and that required by the SN/CSM models of Chiotellis et al. (2012) and Patnaude et al. (2012), who required a distance greater than about 6 kpc.

Using our derived value of the distance, we have calculated the proper motion shock velocities of the filaments. We have estimated the densities in the pre-shock gas from these velocities and the Hα fluxes of the filaments. The distribution of shock velocities and pre-shock densities have been discussed for three components: (i) the main shock along the remnant perimeter, (ii) the shock driven ahead of the ejecta knot, and (iii) the shocks near the center and in the projected interior of the remnant.

Our revised distance to Kepler, and the shock velocity and density estimates provide information that can strongly guide and constrain hydrodynamic models of the supernova blast wave interaction with the CSM around the progenitor star.

We thank Derek Hammer (previously of STScI) for his expertise with the AstroDrizzle package and providing us with the final aligned, CTE-corrected images used for analysis. Figures 9 and 10 were made using Veusz, a scientific plotting package written by Jeremy Sanders. This work was supported in part by NASA Grant HST-GO-12885 awarded to the Universities Space Research Association and to the Johns Hopkins University.

Facilities: Hubble Space Telescope.

REFERENCES

Baade, W. 1943, ApJ, 97, 119

Bandiera, R. 1987, ApJ, 319, 885

Blair, W. P., Long, K. S., & Vancura, O. 1991, ApJ, 366, 484

Blair, W. P., Ghavamian, P., Long, K. S., et al. 2007, ApJ, 662, 998

Borkowski, K. J., Blondin, J. M., & Sarazin, C. L. 1992, ApJ, 400, 222

Borkowski, K. J., Blondin, J. M., & McCray, R. 1997, ApJ, 477, 281

Burkey, M. T., Reynolds, S. P., Borkowski, K. J., & Blondin, J. M. 2013, ApJ, 764, 63

Cassam-Chenaï, G., Decourchelle, A., Ballet, J., et al. 2004, A&A, 414, 545

Chevalier, R. A., & Raymond, J. C. 1978, ApJ, 225, L27

Chiotellis, A., Schure, K. M., & Vink, J. 2012, A&A, 537, AA139

DeLaney, T., Koralesky, B., Rudnick, L., & Dickel, J. R. 2002, ApJ, 580, 914

Dennefeld, M. 1982, A&A, 112, 215

Dodorico, S., Bandiera, R., Danziger, J., & Focardi, P. 1986, AJ, 91, 1382

Doggett, J. B., & Branch, D. 1985, AJ, 90, 2303

Douvion, T., Lagage, P. O., Cesarsky, C. J., & Dwek, E. 2001, A&A, 373, 281

Fesen, R. A., Becker, R. H., Blair, W. P., & Long, K. S. 1989, ApJ, 338, L13

Field, J. V., Postl, A., & Kepler, J. 1977, Vistas in Astronomy, 20, 333

Fruchter, A. S., Hack, W., Dencheva, N., Droettboom, M., & Greenfield, P. 2010, Space Telescope Science Institute Calibration Workshop Proceedings, eds. S. Deustua & C. Oliveira, (Baltimore: STScI).

Ghavamian, P., Raymond, J., Smith, R. C., & Hartigan, P. 2001, ApJ, 547, 995

Ghavamian, P., Winkler, P. F., Raymond, J. C., & Long, K. S. 2002, ApJ, 572, 888

Ghavamian, P., Laming, J. M., & Rakowski, C. E. 2007, ApJ, 654, L69

Gonzaga, S., Hack, W., Fruchter, A., & Mack, J. eds. 2012, The DrizzlePac Handbook (Baltimore: STScI).

Heng, K., van Adelsberg, M., McCray, R., & Raymond, J. C. 2007, ApJ, 668, 275

Kerzendorf, W. E., Childress, M., Scharwächter, J., Do, T., & Schmidt, B. P. 2014, ApJ, 782, 27

Kinugasa, K., & Tsunemi, H. 1999, PASJ, 51, 239

Laming, J. M., Raymond, J. C., McLaughlin, B. M., & Blair, W. P. 1996, ApJ, 472, 267

Leibowitz, E. M., & Danziger, I. J. 1983, MNRAS, 204, 273

Masci, F. 2013, Astrophysics Source Code Library, 1302.010

Morlino, G., Blasi, P., Bandiera, R., & Amato, E. 2013, A&A, 558, A25

Patnaude, D. J., Badenes, C., Park, S., & Laming, J. M. 2012, ApJ, 756, 6

Raymond, J. C., Korreck, K. E., Sedlacek, Q. C., et al. 2007, ApJ, 659, 1257

Raymond, J. C., Ghavamian, P., Williams, B. J., et al. 2013, ApJ, 778, 161

Raymond, J. C., Edgar, R. J., Ghavamian, P., & Blair, W. P. 2015, ApJ, 805, 152

Reynolds, S. P., Borkowski, K. J., Hwang, U., et al. 2007, ApJ, 668, L135

Reynoso, E. M., & Goss, W. M. 1999, AJ, 118, 926

Sankrit, R., Blair, W. P., Delaney, T., et al. 2005, Advances in Space Research, 35, 1027

Sankrit, R., Blair, W. P., Frattare, L. M., et al. 2008, AJ, 135, 538

Shimoda, J., Inoue, T., Ohira, Y., et al. 2015, ApJ, 803, 98

Toledo-Roy, J. C., Esquivel, A., Velázquez, P. F., & Reynoso, E. M. 2014, MNRAS, 442, 229

van Adelsberg, M., Heng, K., McCray, R., & Raymond, J. C. 2008, ApJ, 689, 1089

van den Bergh, S., & Kamper, K. W. 1977, ApJ, 218, 617

Williams, B. J., Borkowski, K. J., Reynolds, S. P., et al. 2012, ApJ, 755, 3

Yamaguchi, H., Badenes, C., Petre, R., et al. 2014, ApJ, 785, L27

This preprint was prepared with the AAS LaTeX macros v5.2.

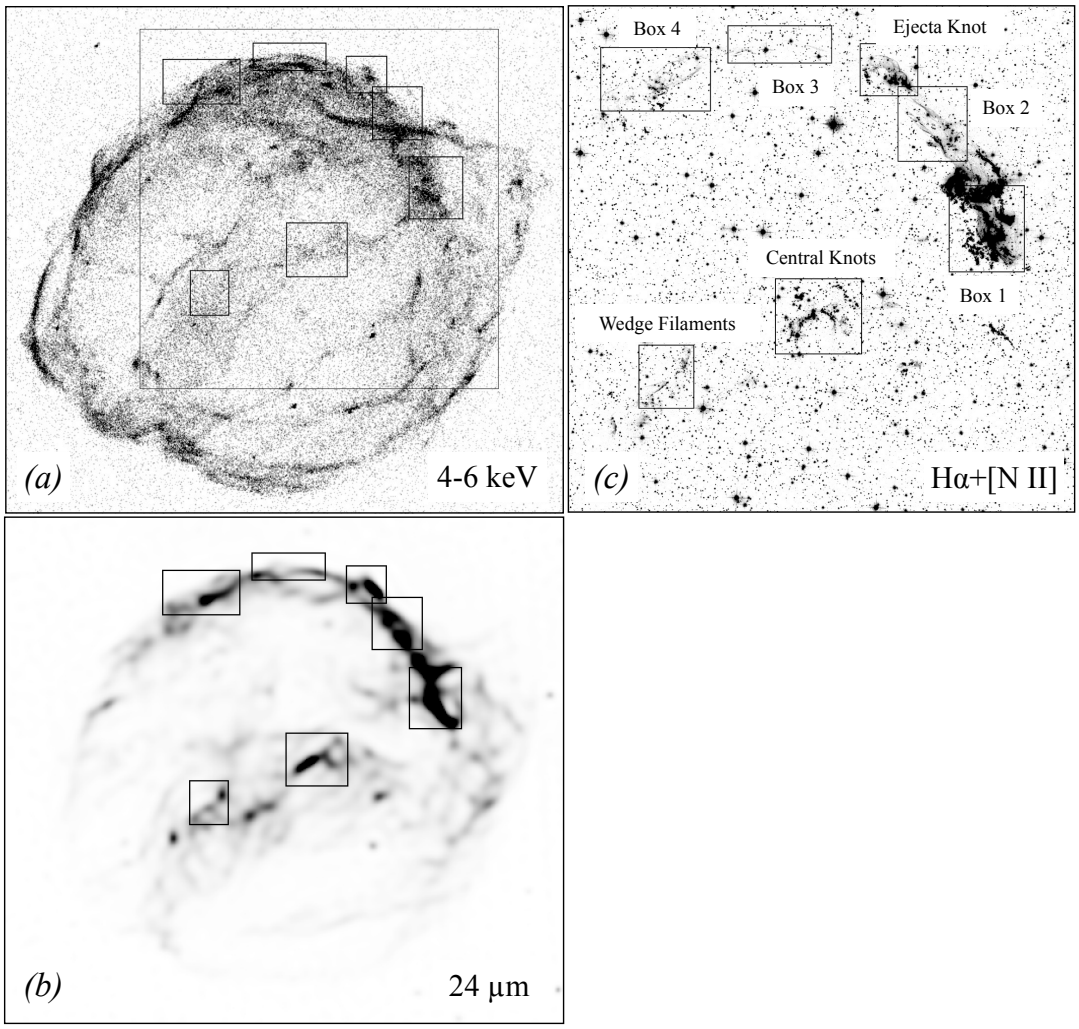

Fig. 1.— *(a):* *Chandra* image of Kepler. The 4–6 keV channel shows primarily the non-thermal emission. The field of view is $270'' \times 246''$, with north up and east to the left. *(b):* Deconvolved *Spitzer* MIPS 24μm image, with the same field of view as the X-ray image. *(c):* HST/ACS F658N (Hα+[N II]) image of Kepler obtained in 2003. The field of view is $175'' \times 175''$ and corresponds to the larger box shown on the X-ray image. In all three panels, the smaller boxes outline regions of interest that will be discussed in this paper. We will refer to these regions using the labels shown on the optical image.

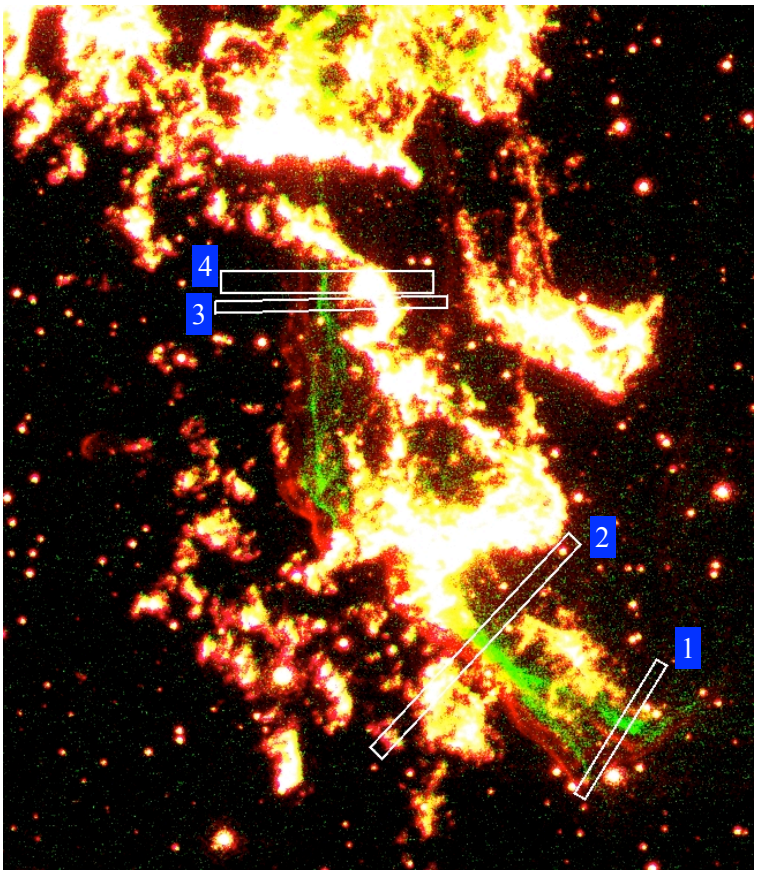

Fig. 2.— Three-color image of the Box 1 region. The ACS F658N image showing epoch 1 Hα+[N II] is in red, the WFC3 F656N image showing epoch 2 Hα is in green, and the ACS F660N image showing epoch 1 [N II] only is in blue. The red and green features are the Balmer filaments (only Hα emission) in epoch 1 and epoch 2, respectively. Radiative shocks show up as white, and in some regions as yellow due to the stretch used in the display. Stars are white. The cuts along which the proper motions were measured are shown along with labels used in the text and in Table 1. The image dimensions are about $26'' \times 30''$.

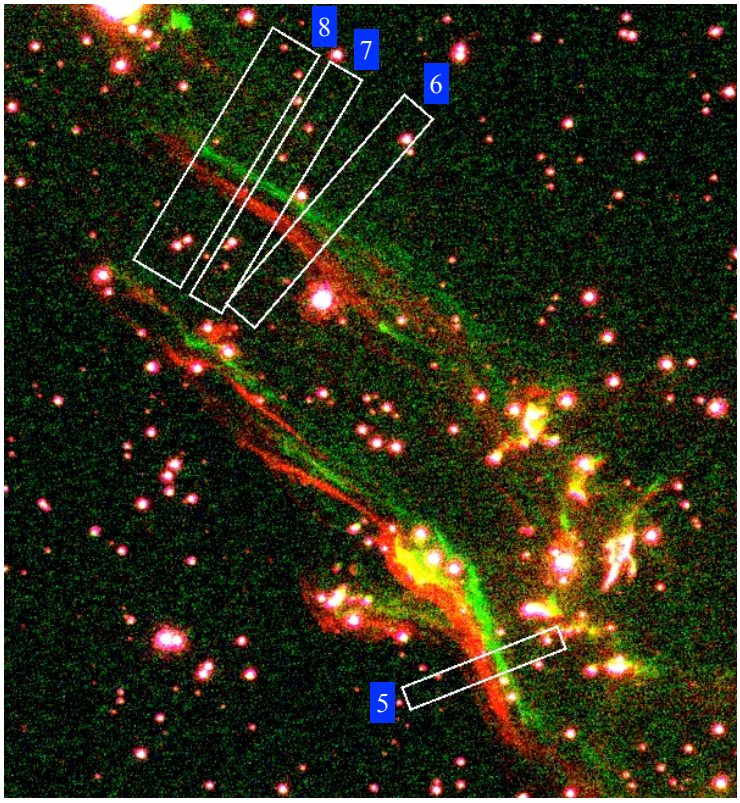

Fig. 3.— The same as Figure 2 for Box 2. The image dimensions are about $24'' \times 26''$.

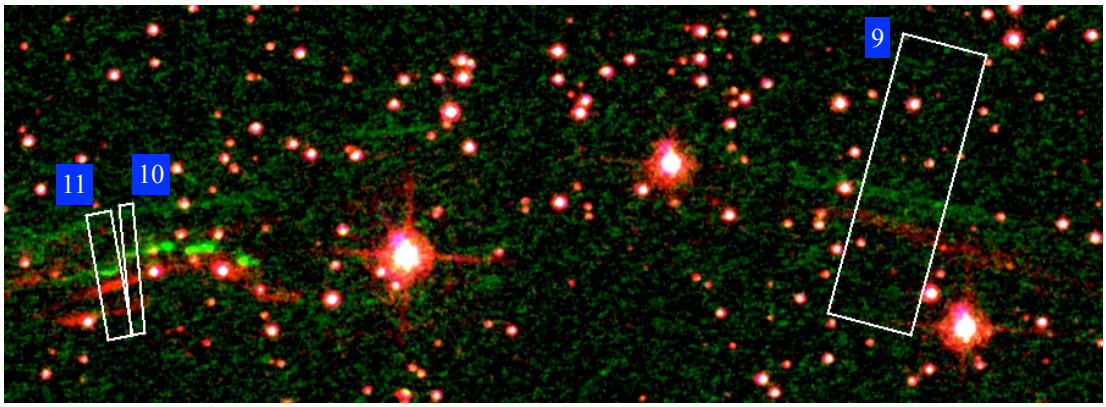

Fig. 4.— The same as Figure 2 for Box 3. In this case, the images have been smoothed by 2×2 pixel FWHM gaussian. The image dimensions are about $36'' \times 13''$.

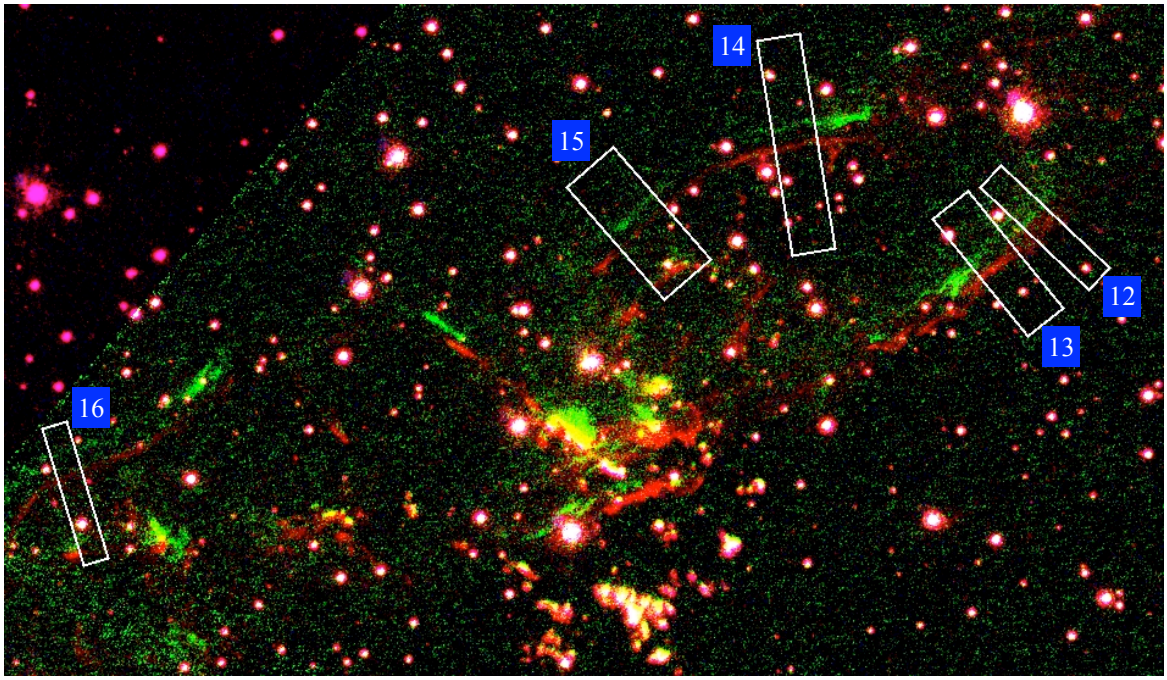

Fig. 5.— The same as Figure 2 for Box 4. The image dimensions are about $38'' \times 22''$.

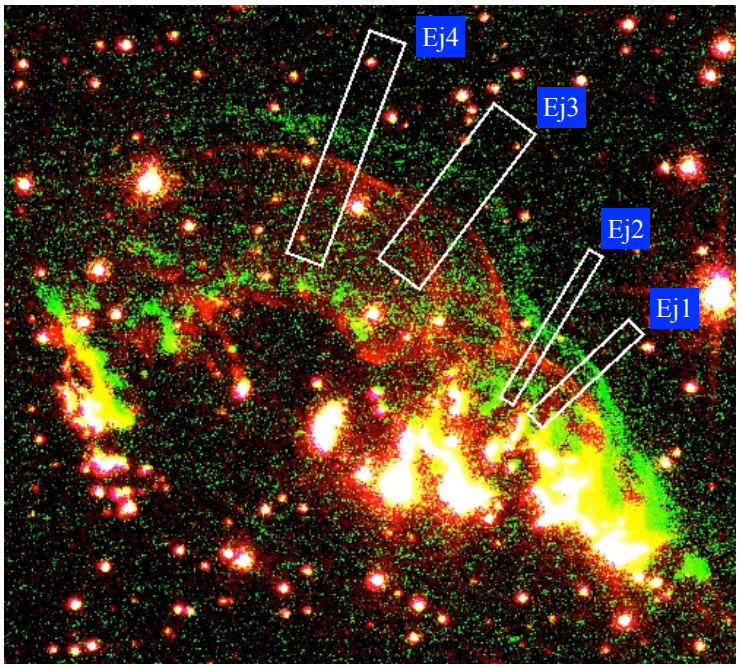

Fig. 6.— The same as Figure 2 for the Ejecta Knot. The image dimensions are about $20'' \times 18''$.

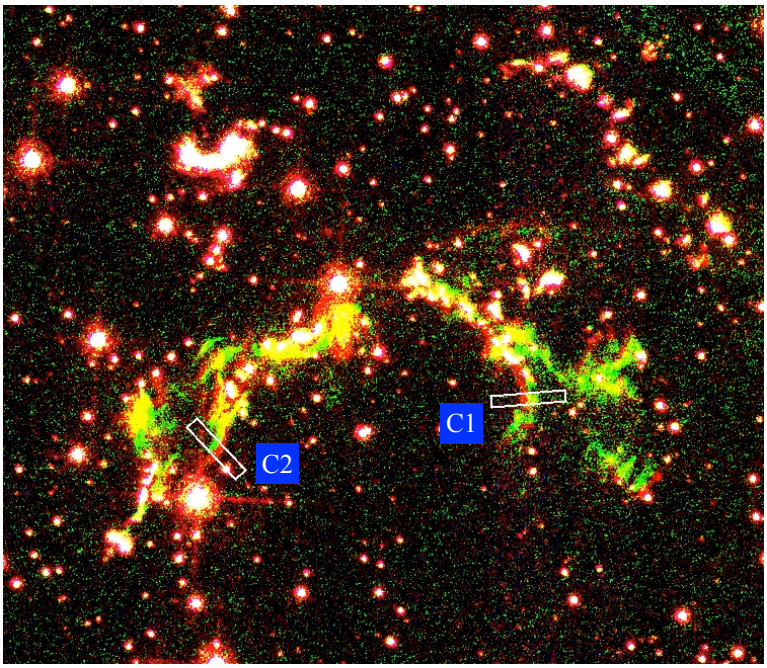

Fig. 7.— The same as Figure 2 for the Central knots. The image dimensions are about $30'' \times 26''$.

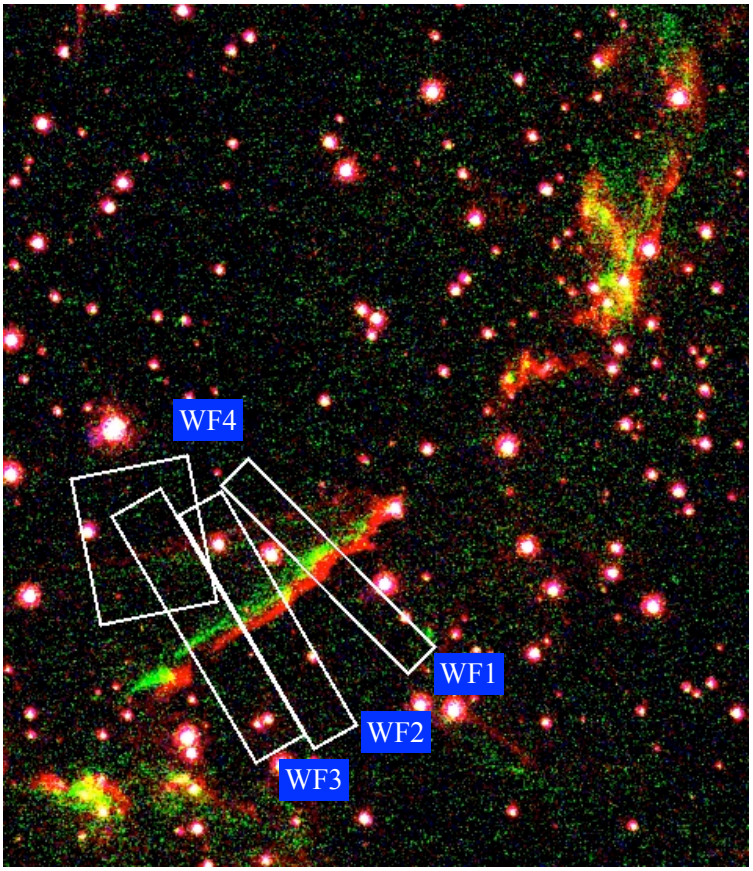

Fig. 8.— The same as Figure 2 for the Wedge Filaments. The image dimensions are about $19'' \times 22''$.

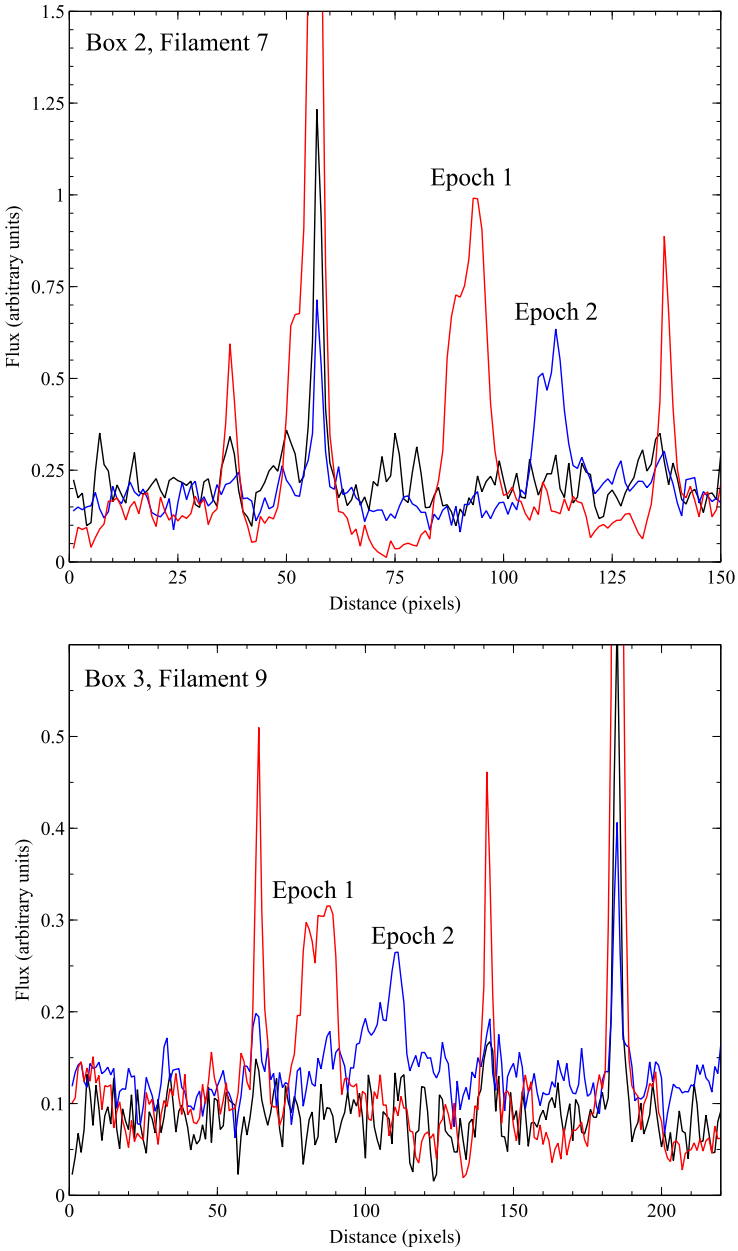

Fig. 9.— Hα emission profiles across Balmer line filaments. Top panel: filament 7 in Box 2 (Fig. 3); bottom panel: filament 9 in Box 3 (Fig. 4). In red is the epoch 1 ACS F658N emission, in blue is the epoch 2 WFC3 F656N emission, and in black is the epoch 1 ACS F660N emission, which is essentially zero except at the location of the stars. The labels, "Epoch 1" and "Epoch 2" in each of the panels show the locations of the Balmer filament in 2003 and 2013, respectively.

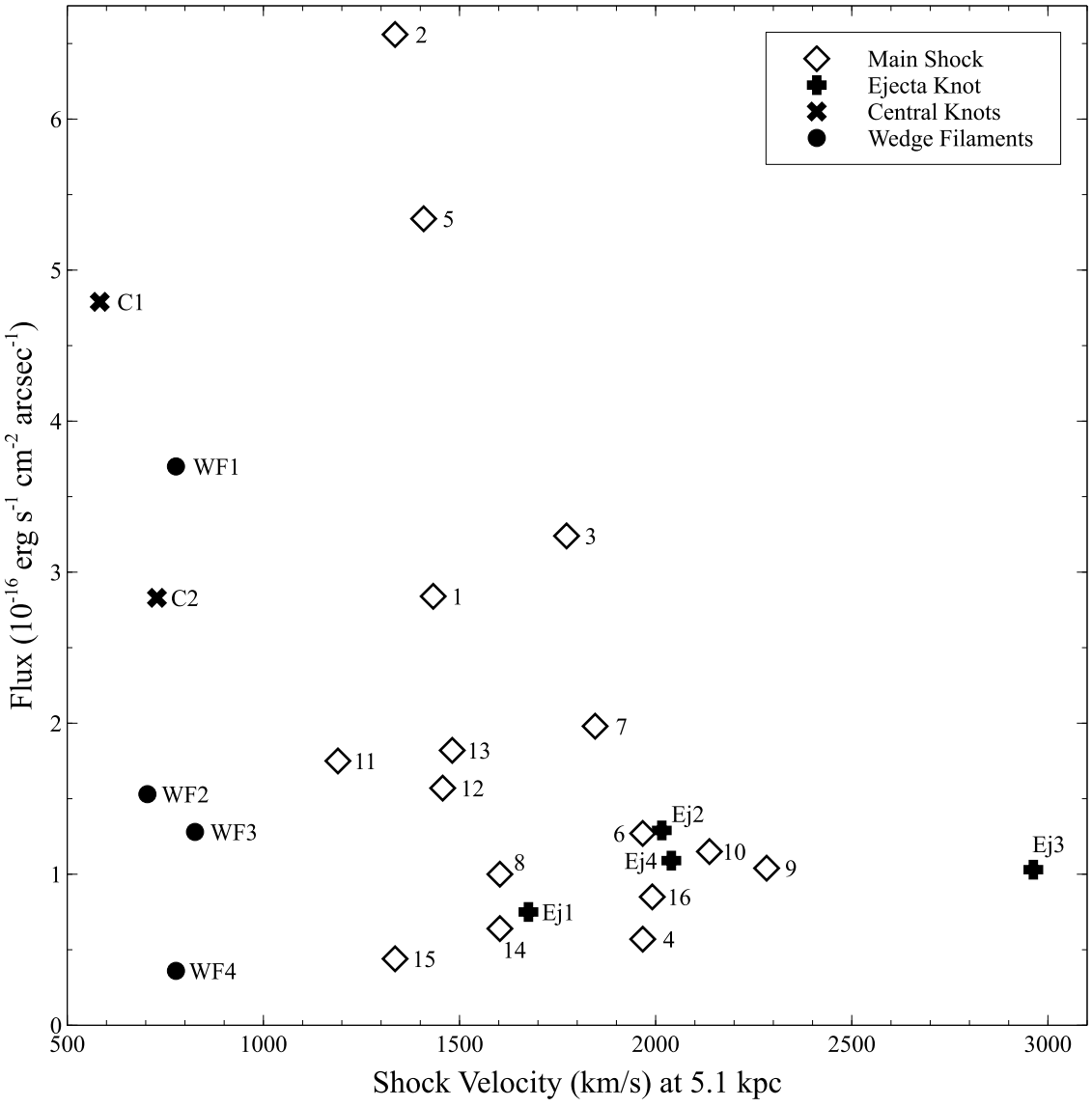

Fig. 10.— The Hα emission peak intensities are plotted against the proper motion shock velocities obtained assuming a distance of 5.1 kpc to Kepler. The intensity and proper motion values are from Table 1, as are the labels used for each point.

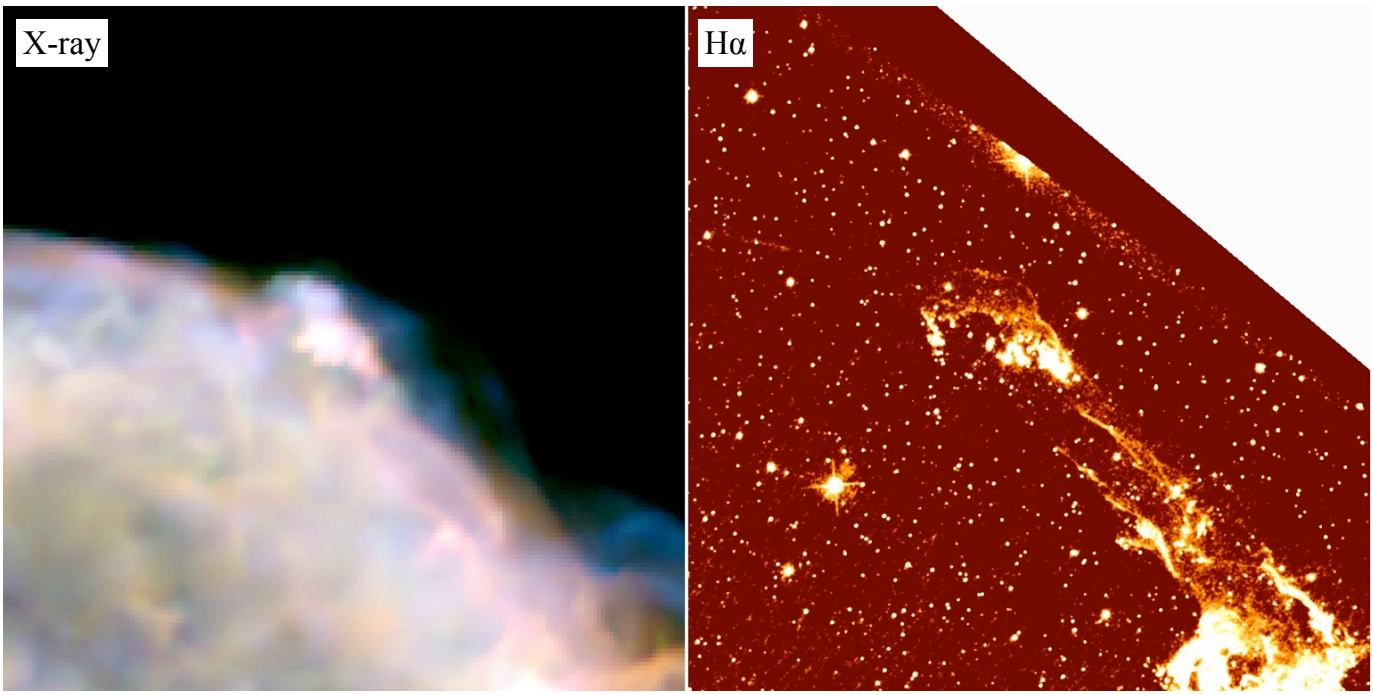

Fig. 11.— The region around the ejecta knot. Left: A smoothed three-color *Chandra* image with 0.3–0.72 keV emission in red, 0.72–1.7 keV in green and 1.7–7.0 keV in blue. Right: HST/WFC3 F656N (Hα) image. The field of view shown is an $82'' \times 88''$.

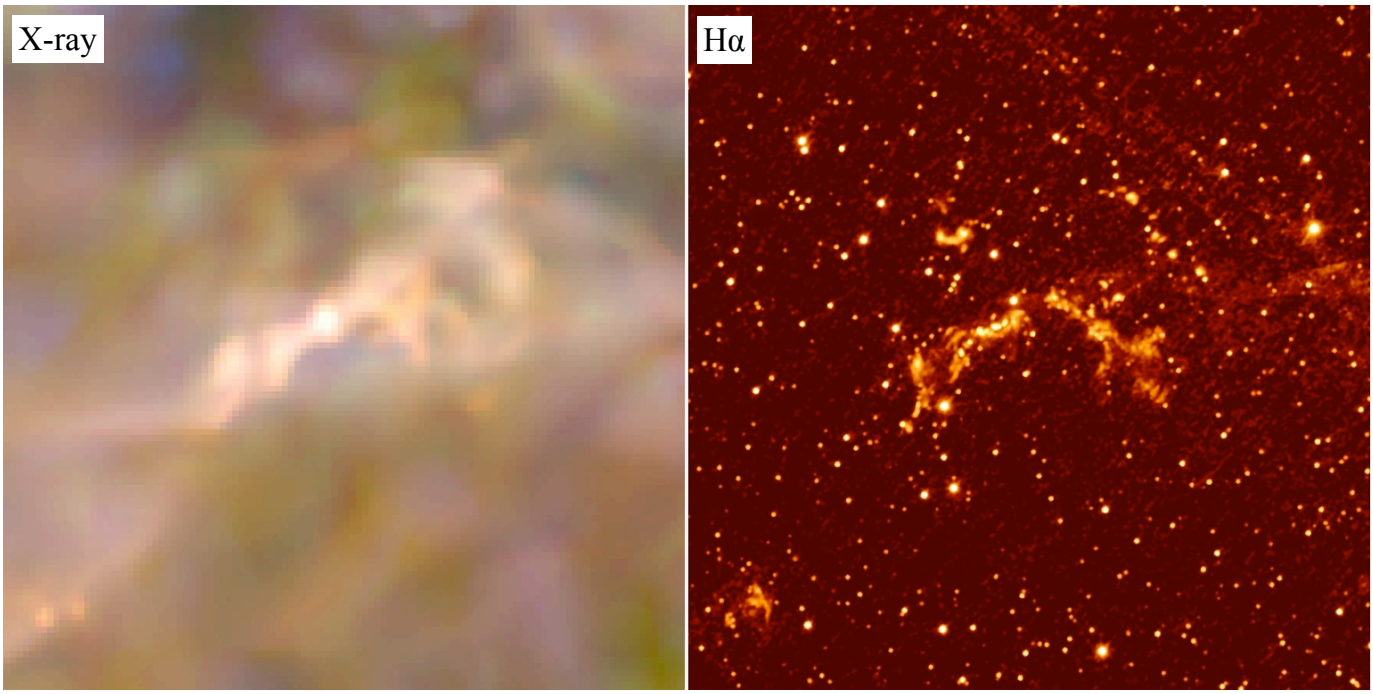

Fig. 12.— The same as Figure 11, for a $50'' \times 50''$ region around the Central Knots.

Table 1. Balmer Filament Properties

Filament	α_{J2000} ; δ_{J2000}	Box Width	$\Delta\Theta/\Delta\,t$	I_{peak}	FWHM
1	17:30:35.37 ; −21:29:01.1	10.5	0.059	15.6	0.″17
2	17:30:35.73 ; −21:28:58.2	14.2	0.055	20.5	0.″30
3	17:30:36.14 ; −21:28:46.2	10.4	0.073	7.8	0.″39
4	17:30:36.15 ; −21:28:45.5	19.3	0.081	3.9	0.″14
5	17:30:37.03 ; −21:28:23.4	19.0	0.058	15.6	0.″32
6	17:30:37.45 ; −21:28:09.7	30.2	0.081	5.9	0.″20
7	17:30:37.54 ; −21:28:08.5	29.8	0.076	8.8	0.″21
8	17:30:37.65 ; −21:28:07.5	44.2	0.066	4.9	0.″19
9	17:30:40.25 ; −21:27:48.1	70.5	0.094	2.0	0.″50
10	17:30:42.03 ; −21:27:49.9	10.9	0.088	4.9	0.″22
11	17:30:42.08 ; −21:27:50.1	20.5	0.049	7.8	0.″21
12	17:30:43.04 ; −21:27:55.8	24.2	0.060	2.9	0.″50
13	17:30:43.15 ; −21:27:57.0	37.1	0.061	5.9	0.″29
14	17:30:43.62 ; −21:27:53.1	35.8	0.066	2.9	0.″21
15	17:30:43.97 ; −21:27:55.8	50.7	0.055	2.0	0.″21
16	17:30:45.31 ; −21:28:03.8	20.4	0.082	2.0	0.″41
Ej1	17:30:37.97 ; −21:27:57.4	14.1	0.069	3.9	0.″18
Ej2	17:30:38.05 ; −21:27:56.7	10.6	0.083	6.8	0.″18
Ej3	17:30:38.21 ; −21:27:52.7	34.9	0.122	2.0	0.″50
Ej4	17:30:38.42 ; −21:27:51.4	25.2	∼0.08[a]	5.9	0.″18
C1	17:30:39.70 ; −21:29:23.4	11.0	0.024	11.7	0.″39
C2	17:30:40.56 ; −21:29:25.5	13.1	0.030	9.8	0.″27
WF1	17:30:43.93 ; −21:29:44.9	23.7	0.032	15.6	0.″22
WF2	17:30:44.04 ; −21:29:46.2	30.6	0.029	8.8	0.″16
WF3	17:30:44.12 ; −21:29:46.8	35.0	0.034	4.9	0.″25

Table 1—Continued

Filament	α_{J2000} ; δ_{J2000}	Box Width	$\Delta\Theta/\Delta\,t$	I_{peak}	FWHM
WF4	17:30:44.25 ; −21:29:44.6	75.8	0.032	2.0	$0\farcs18$

Note. — The columns are as follows – (1) filament label used in the text and figures, (2) approximate co-ordinates of the filament in the 2003 ACS image, (3) width, in pixels, of the extraction boxes, (4) filament proper motion, in arcsec/yr, (5) Peak intensity of the filament profile in the Epoch 1 data in units of 10^{-16} erg s^{-1} cm^{-2} $arcsec^{-2}$ and (6) full-width-half-maximum of the filament profile in the Epoch 1 data.

[a]Approximate value; the uncertainty in the measured displacement is ∼2 pixels.